

Sequential Estimator: Toward Efficient InSAR Time Series Analysis

Homa Ansari, *Student Member, IEEE*, Francesco De Zan, and Richard Bamler, *Fellow, IEEE*

Abstract—Wide-swath synthetic aperture radar (SAR) missions with short revisit times, such as Sentinel-1 and the planned NISAR and Tandem-L, provide an unprecedented wealth of interferometric SAR (InSAR) time series. However, the processing of the emerging Big Data is challenging for state-of-the-art InSAR analysis techniques. This contribution introduces a novel approach, named *Sequential Estimator*, for efficient estimation of the interferometric phase from long InSAR time series. The algorithm uses recursive estimation and analysis of the data covariance matrix via division of the data into small batches, followed by the compression of the data batches. From each compressed data batch artificial interferograms are formed, resulting in a strong data reduction. Such interferograms are used to link the “older” data batches with the most recent acquisitions and thus to reconstruct the phase time series. This scheme avoids the necessity of reprocessing the entire data stack at the face of each new acquisition. The proposed estimator introduces negligible degradation compared to the Cramér–Rao lower bound under realistic coherence scenarios. The estimator may therefore be adapted for high-precision near-real-time processing of InSAR and accommodate the conversion of InSAR from an offline to a monitoring geodetic tool. The performance of the Sequential Estimator is compared to state-of-the-art techniques via simulations and application to Sentinel-1 data.

Index Terms—Big Data, coherence estimation error, data compression, differential interferometric synthetic aperture radar (DInSAR), distributed scatterers, efficiency, error analysis, low-rank approximation, maximum-likelihood estimation (MLE).

ACRONYMS

CCG	Complex circular Gaussian.
CRLB	Cramér–Rao lower bound.
DS	Distributed scatterer.
EVD	Eigenvalue decomposition.
MLE	Maximum-likelihood estimation.
NRT	Near-real-time.
PCA	Principal component analysis.
PS	Persistent scatterer.
RMS	Root mean square.
SBAS	Small-baseline subset approach.
StBAS	Short temporal-baseline subset.
SLC	Single-look complex.

Manuscript received December 13, 2016; revised April 12, 2017; accepted May 15, 2017. Date of publication September 1, 2017; date of current version September 25, 2017. This work was supported by the ‘Helmholtz Alliance Remote Sensing and Earth System Dynamics’ funded by the Initiative and Networking Fund of the Helmholtz Association. (*Corresponding author: Homa Ansari.*)

H. Ansari and F. De Zan are with the German Aerospace Center, Oberpfaffenhofen, Germany (e-mail: homa.ansari@dlr.de; francesco.dezan@dlr.de).

R. Bamler is with the German Aerospace Center, Germany, and also with the Chair of Remote Sensing Technology, Technical University of Munich, 80333 Munich, Germany (e-mail: richard.bamler@dlr.de).

Color versions of one or more of the figures in this paper are available online at <http://ieeexplore.ieee.org>.

Digital Object Identifier 10.1109/TGRS.2017.2711037

NOTATION

$n \in \mathbb{N}$	Number of the SLCs in the SAR data stack.
$l \in \mathbb{N}$	Number of samples in a statistically homogeneous spatial neighborhood.
$s \in \mathbb{N}$	Number of the SLCs included in the mini-stack.
$m \in \mathbb{N}$	Dimension of the low-rank signal subspace.
$\Omega \in \mathbb{C}^{1 \times l}$	Group of l statistically similar pixels surrounding a single pixel of interest, the interferometric signal is assumed to be stationary within this ensemble.
$Z \in \mathbb{C}^{n \times l}$	Matrix of acquired SLCs, the rows correspond to the images in the stack, the columns to the ensemble of pixels in Ω .
$C \in \mathbb{C}^{n \times n}$	Complex coherence matrix of the stack;
$\Gamma \in \mathbb{R}^{n \times n}$	Coherence matrix of the interferograms defined as $\Gamma_{ij} = C_{ij} $.
$I_{\Omega} \in \mathbb{C}^{n \times n}$	Complex matrix of the interferograms.
$\phi \in \mathbb{C}^{n \times 1}$	Sought phase series in phase-linking, estimated phase of each SLC inclusive of the systematic/deterministic phase components.
A	Capital letter indicating a generic matrix.
A_i	Subscripted capital letter indicating the i th row of the generic matrix A .
b	Small bold letter indicating a generic vector.
$\hat{\cdot}$	Hat accentuation distinguishing an estimated from an observed variable.

I. INTRODUCTION

TIME-SERIES analysis of interferometric synthetic aperture radar (InSAR) has proved to be a high-precision geodetic approach for monitoring the crustal deformation of the earth. The retrieval of the geophysical signal from InSAR data stacks is limited by the atmospheric perturbation as well as the temporal decorrelation of the SAR signal. In the pursuit of overcoming these limitations, the exploitation of InSAR stacks was initially limited to the Persistent Scatterers (PSs) [1], [2]. The PSs are phase-stable scatterers and do not undergo severe temporal decorrelation. Exploiting PSs, the separation of the geophysical signal from the atmospheric perturbations follows in a separate step [1], [2]. Although precise in signal retrieval, the scarcity of PSs in nonurban areas has led the InSAR community toward relaxing the strict limit on the phase stability and including the areas affected by decorrelation, referred to as the distributed scatterers (DSs).

The pioneering DS approach in minimizing the effect of decorrelation was to limit the analysis to subsets of moderate

to high-coherent interferograms, referred to as small-baseline subsets (SBASs) [3], therefore excluding the decorrelated interferometric pairs. Setting an *a priori* threshold on the geometric and temporal baseline, or equivalently on the coherence, the data stack is divided into coherent subsets of interferograms, each subset is then spatially unwrapped. The unwrapped phases of the different subsets are temporally integrated to estimate a phase series inclusive of the geophysical signal of interest.

Improving one step further, the imposed strict coherence limit for the subset selection was relaxed, allowing all interferograms to be properly included in the retrieval of the geophysical signal [4], [5]. The effect of decorrelation in this case is minimized by exploitation of the statistical properties of the interferometric stack in a maximum-likelihood estimation (MLE) scheme. Approximating the mean scattering of DS by a PS-resembling mechanism, the MLE estimates a wrapped phase series which pertains to the superposed systematic phase components. Each element of the series corresponds to an image in the stack and is relative to an arbitrarily fixed master image. Borrowed from Guarnieri and Tebaldini [4], the retrieval of the wrapped phase is hereafter referred to as *phase-linking*. The estimated phase series bears the sought geophysical signature, although superposed by an atmospheric-induced signal. The separation of the atmospheric contribution from the geophysical signal may be followed in a second estimation step as in the case of PSs [1], [2], [4].

The MLE designs a temporal filter adaptive to the coherence, as the second-order statistic of the data. It provides an asymptotically optimum estimator with variance close to the Cramér–Rao lower bound (CRLB) [4], [6]. If unknown, the coherence is substituted by its estimation. The MLE is therefore bound to the performance of the coherence estimation. The well-known suboptimality of the coherence estimation [7], [8] is the major limitation for MLE to reach its asymptotic behavior. In the case of poor performance of the coherence estimator, the MLE may be shown to deviate largely from the CRLB; hence, its optimality is compromised (see Section VI-C, [9], [10]).

Building on the MLE, the estimation of the geophysical signal has been further investigated by substitution of the ML optimization by robust M-estimators [11] or integer least squares [10]. The former aims at increasing the *accuracy* of phase-linking by addressing special cases where the data characteristics deviate from the assumed stationary Complex Circular Gaussian (CCG) statistics in MLE; the latter primarily focuses on the addition of an *a posteriori* quality indicator of the estimated phases.

A second category of phase-linking based on the exploitation of all interferometric pairs was first proposed in [12] and later in [13]. It primarily focuses on the extraction of the scattering mechanisms of the DS through eigenvalue decomposition (EVD) of the data covariance matrix. Compared to the MLE, it relaxes the single-dyadic (i.e., PS-resembling) approximation of the DS-scattering mechanism and allows the retrieval of the decomposed phase signature with multiple dyads of different power. However,

having a performance deviant from the CRLB [9], [10] in generic cases, the EVD is a suboptimum phase estimator.

Despite their various implementation details, all DS techniques rely on the analysis of the complex coherence matrix of the data stack. Estimated from the time series, the complex coherence is a Hermitian matrix containing all possible interferograms as well as their respective coherence. It is comprised of the total number of $n(n - 1)/2$ unique entities, with n being the number of single-look complex (SLC) images in the data stack. The formation and exploitation of the full coherence matrix can, however, be computationally demanding, especially in large data stacks. The computational burden increases at least cubically with the dimension of the data at hand.

The current and future spaceborne SAR missions with systematic earth monitoring objective tend to follow the wide-swath design with revisit cycle as low as possible to allow for high temporal resolution monitoring of the earth. With missions such as ESA's Sentinel-1 or, in the near future, NASA's NISAR, the short revisit of 6–12 days gives birth to unprecedented SAR data volumes. The interferometric processing of such emerging Big Data stacks with the current available DS algorithms would be infeasible, especially if systematic high-precision near-real-time (NRT) monitoring of even small earth surface motion is the objective. The NRT processing will open a new chapter in InSAR applications, converting the method from an offline analysis mode to a high-precision nearly online monitoring tool with applications, e.g., in early warning systems.

The InSAR community has recently commenced addressing this new demand [14]–[17]. However, in the recent attempts, the focus is mostly on the automation of the SAR data acquisition and optimization of the processing prior to the time series analysis. As of present, the main attempt has been on the reduction of the product latency through parallelized computation and improvement of the computational capacity, e.g., via cloud computing. Being an inherently nonparallel problem, the core time series analysis techniques have been left intact. As briefly reported, Heu *et al.* [14] and Gonzalez *et al.* [15] exploit SBAS-like techniques in retrieval of the geophysical signal while Adam *et al.* [16] is tailored to the PSs. Although sufficient for retrieval of large-scale deformation, the SBAS approach fails in efficient processing of large data stacks. In defining the efficiency, two distinct criteria are distinguished here, namely, the algorithmic efficiency, i.e., the processing run time; and the estimation efficiency, i.e., the optimality of the estimator with respect to the CRLB. The algorithmic efficiency of SBAS may be improved by restricting the temporal baseline and exploiting a limited subset of interferograms. However, such restrictions compromise the estimation efficiency and consequently degrade the sensitivity to small surface motions. Hereafter, efficiency implies both the algorithmic and estimation optimality criteria.

The idea of an efficient stacking technique was raised for the first time by De Zan and López-Dekker [18]. Proposing a technique tailored to a special coherence scenario, termed long-term coherence, the authors succeeded in retaining performance close to the CRLB while avoiding the full

exploitation of the entire data stack. The scheme, however, fails in the absence of the long-term coherence.

Inspired by De Zan and López-Dekker [18], this contribution proposes a novel generic efficient stacking technique, named the Sequential Estimator. The proposed approach allows efficient phase-linking in sequences by using isolated data batches of the time series. It thus avoids the necessity to access the entire time series at each processing sequence and refrains from reprocessing the entire data archive at the face of each new SAR acquisition. Compressing the isolated data batches and generating artificial interferograms with the compressed data, the Sequential Estimator retains a performance close to the CRLB. The method competes with expensive full-stack phase-linking techniques and even outperforms them in case the exploited estimation of coherence is suboptimum.

To the best of our knowledge, the Sequential Estimator is the first proposal for a generic efficient InSAR stacking in the realm of DS. The algorithm provides a recursive solution to the temporally nonparallelizable problem of phase-linking. The proposed estimator may be combined with the optimized wide area processing techniques in [16] and [19], and therefore contribute to the state-of-the-art automatic InSAR processing in the pursuit of high-precision NRT earth deformation monitoring.

In the following, a short introduction of the possible optimized stacking schemes is provided in Section II. The description of the Sequential Estimator starts from Section III, where the compression technique used for the SAR data stack is elaborated; further algorithmic steps are described in Section IV. Section V highlights the computational gain of the scheme. Finally, the performance of the estimator is assessed through simulations and application to Sentinel-1 data in Sections VI and VII, respectively.

II. CONVENTIONAL VERSUS AGILE PHASE-LINKING

This section starts from laying down the formulation of the phase-linking which is used throughout this paper. The MLE phase-linking as well as possible agile, i.e., computationally light, stacking techniques are introduced. As it will be shown through simulations (see Section VI-C), the introduced techniques are inefficient, in the sense that their optimality is compromised by the introduced limit on data accessibility. The review of these alternative schemes is, however, worthwhile to highlight the encountered challenges for an efficient stacking method.

Note that the spatial analysis is always considered pixel wise throughout this paper, although the statistics of each single pixel is inferred from an ensemble of pixels belonging to a statistically homogeneous region, hereafter referred to as the Ω neighborhood.

A. Conventional MLE Phase-Linking: Full Accessibility to the Stack

The MLE scheme exploits the complex coherence matrix to estimate the phase series inclusive of the geophysical signal. The complex coherence matrix of the data stack is estimated

using an ensemble of l pixels in statistically homogeneous neighborhoods. The statistical homogeneity of the chosen ensemble is assured via statistical similarity tests between the centering and neighboring pixels [5], [20]. Sorting the chosen ensemble in a spatiotemporal data matrix Z , the MLE of complex coherence matrix reads as

$$\hat{C} = \frac{ZZ^H}{\sqrt{[[Z]]^2([Z]]^2)^T}} \quad (1)$$

where $[[Z]]$ gives the column-wise $L2$ norm of the matrix Z , the power-2 and deviation operations are element wise. \hat{C} is an $n \times n$ matrix that encapsulates the available interferometric information with its argument containing the interferometric phases and its modulus $\hat{\Gamma}$ providing an estimate of the coherence of the corresponding interferograms. Under the assumption of the CCG statistics, the MLE of phase is retrieved via [4]

$$\hat{\phi}_{ML} = \operatorname{argmin}_{\phi} \{ \hat{\xi}_{ML}^H (\hat{\Gamma}^{-1} \circ \hat{C}) \hat{\xi}_{ML} \} \quad (2)$$

here \circ is the Hadamard operation and $\hat{\xi}_{ML}$ is a vector containing the sought phase of each SLC with its elements set to $\exp(j\phi_i)$. With this assumed model, the scattering behavior of the DS neighborhood is approximated by a PS-resembling mechanism. The MLE may be interpreted as a temporal filter that compresses the information of $n(n-1)/2$ interferograms to a phase series of size n .

B. Alternative Agile Phase-Linking Schemes: Partial Accessibility to the Stack

The first requirement for an efficient stacking scheme is to avoid reprocessing and rereading the entire data history when encountering a new acquisition. To fulfill this requirement, the intuitive solution is to follow the footsteps of SBAS with a slight modification: merely allowing the short temporal-baseline interferogram in the phase retrieval. This approach is hereafter referred to as the short temporal-BASeline subset (StBAS). Inspired by Rocca [21] and assuming an exponential decrease of coherence in SAR stack, StBAS exploits successive SLCs with temporal separation up to an *a priori* time lag. The StBAS interferograms are combined via MLE phase-linking. Compared to the conventional MLE, here a banded matrix replaces the full coherence matrix. The bandwidth of the matrix is fixed by the *a priori* time lag. Although straightforward, there are three fundamental problems to this approach as follows.

- 1) At each processing step, up to a certain lag of the previously acquired data shall be reread and reprocessed, i.e., the proposed stacking method still undergoes redundant computations.
- 2) The choice of the *a priori* temporal baseline imposes a trade-off between the estimation efficiency and the computational burden, i.e., to avert exclusion of the coherent interferograms and the consequent performance degradation of the estimator, a longer time lag is required.
- 3) StBAS assumes that the interferograms with temporal baselines of larger than the time lag bear no coherent signal. This assumption loses validity in explaining seasonal decorrelation or long-term coherence observed for C- and L-bands SAR [23], [24].

To address some of the aforementioned problems, an alternative approach may be taken that emphasizes the long-term, and possibly weak, coherent signals rather than the short-term, high-coherence interferometric pairs. This has been introduced in [18], where the authors suggest using two subsets of the SLCs and retrieving the long-term coherent signal from filtered version of the two subsets. Allowing each subset as $Z_s \in \mathbb{C}^{s \times l}$ with $s \ll n/2$, its filtering follows from exploiting the MLE-estimated phase series $\hat{\phi}_s$ via

$$\hat{v}_s(q) = \frac{1}{S} \sum_{p=1}^s Z_s(p, q) \exp(-j\hat{\phi}_s(p)). \quad (3)$$

Here, q is the spatial index from 1 to l , indicating that the proposed filter is temporal and not spatial. Termed virtual image v_s is a filtered SLC representing the subset. Exploiting two virtual images at the beginning and end of the stack, a coherent interferogram may be formed which bears the sought long-term coherent signal and provides an estimation of the phase between the first and last SLC. The performance of this approach is, however, compromised if no coherent signal is present among the chosen subsets. This method is hereafter referred to as *virtual image estimator*.

In pursuit of an efficient stacking technique, the shortcomings of both StBAS and the virtual image estimator shall be conquered. An efficient estimator shall provide a generic solution that properly exploits both the short- and the long-term coherence. To do so, it must be able to adaptively include both weak and strong coherent signals, precisely as does the MLE.

The Sequential Estimator is able to meet a balance between the aforementioned processing regimes. In fact, it may be seen as a generalization of the virtual image estimator that follows the same idea of filtering, or better compressing the information, of the subsets, but without the emphasis on the long-term coherence. Prior to the description of the algorithm, the SAR data compression is explained in Section III.

III. MULTIPASS SAR DATA COMPRESSION

Data compression is a classic approach in dealing with high data volumes. In the case of multipass SAR, the objective is to compress a stack of coregistered SAR data in the temporal direction, such that the size of the time series is reduced but the spatial size of each image is intact. Performed locally, the compression is adaptive to the time series at each resolution cell. The temporal compression is valid since despite the high dimensionality of the data, the prevailing scattering mechanism spans a much lower dimension (see Section IV-A). The introduction of this low-rank signal subspace is the aim of this section.

As a common compression technique, the linear transformations are chosen here. The transforms are mathematically straightforward and computationally efficient, hence well suited to an efficient stacking technique. They provide a mapping from the high-dimensional data space, defined by the row space of $Z^{n \times l}$, to a lower-rank subspace spanning the row space of $\tilde{Z}^{m \times l}$. The linear mapping under a transformation

basis T reads as

$$T : Z^{n \times l} \rightarrow \tilde{Z}^{m \times l} \quad (4)$$

where n is the dimension of data and m is the reduced dimension of its compressed version. Note that the compression is temporal and l as the size of the spatial neighborhood Ω is intact. The transformation T may be defined by any arbitrary set of orthonormal vectors, e.g., Fourier and wavelet bases. The efficiency of the compression is driven by the choice of the basis. In the most efficient case, the basis is chosen to capture the maximum variation of the data space, i.e., by a subset of the most powerful eigenvectors, such that

$$T = \{\mathbf{v}_1; \dots; \mathbf{v}_m\} \quad (5)$$

with the basis vectors derived from the EVD

$$\hat{C}^n = \sum_{p=1}^n \lambda_p \mathbf{v}_p \mathbf{v}_p^H. \quad (6)$$

Here, \hat{C}^n is the complex coherence matrix estimated by substitution of $Z^{n \times l}$ in (1), λ_i are the eigenvalues in descending order and \mathbf{v}_i are the corresponding eigenvectors. This setup is the well-known principal component analysis (PCA) [25], exploited in [12], [13], and [26]. PCA provides a spectral decomposition of the data space, such that the eigenvector corresponding to the highest eigenvalue represents the underlying most coherent signal and vice versa.

The estimation of most coherent signal component \mathbf{v}_1 via generic PCA may be interpreted as [13]

$$\mathbf{v}_1 = \operatorname{argmax}_{\mathbf{v}_1} \{\mathbf{v}_1^H \hat{C}^n \mathbf{v}_1\} \quad (7)$$

subject to $\mathbf{v}_1^H \mathbf{v}_1 = 1$. In this way, PCA approximates the complex coherence matrix with the single dyad $\mathbf{v}_1 \mathbf{v}_1^H$. Being a geometrical rather than a probabilistic approach, PCA fails to correctly incorporate the statistical properties of the data stack; nevertheless, it provides a fair approximation of the phase signature. The MLE, on the other hand, is a purely probabilistic approach. Starting from the CCG assumption and trusting the coherence as the true statistic of the data stack, it formulates the correct metric for phase estimation as the Hadamard product of $\hat{\Gamma}^{-1} \circ \hat{C}$ in (2) and allows the sought dyad of $\hat{\xi} \hat{\xi}^H$, to merely explain the interferometric phases rather than the amplitude variations. The power of PCA is in the decomposition of the probable multiple coherent scattering mechanisms rather than providing precise estimation to the phase-linking. Thus, in the interest of retaining estimation precision, the dyad provided by ML is preferred over the one of the PCA.

Following this rationale, a new orthonormal basis is sought, where its first component is defined as the normalized ML-estimated signal of (2), that is

$$\mathbf{v}_{\text{ML}} = \frac{\exp(j\hat{\phi}_{\text{ML}})}{\|\exp(j\hat{\phi}_{\text{ML}})\|}. \quad (8)$$

\mathbf{v}_{ML} replaces the first component in (5), now the complementary components of this basis are desired. In order to form an orthonormal basis, these components shall span the orthogonal

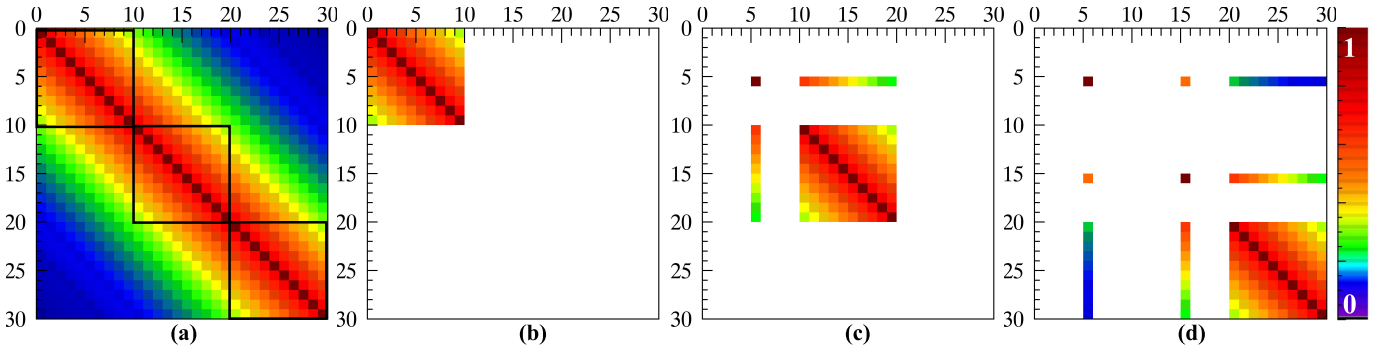


Fig. 1. Schematic depiction of the Sequential Estimator by the coherence matrix. a) Full coherence matrix of a stack of SLCs: the Sequential Estimator divides the stack into isolated mini-stacks indicated by the transparent boxes along the diagonal. At each sequence, one mini-stack is processed and compressed; the mini-stacks are replaced by their compressed components in further sequences. The coherent signals among the mini-stacks are retrieved by generation of artificial interferograms. b) Coherence matrix at the initial sequence. c) Second sequence: the isolated dot on the diagonal indicates the compressed SLC of the unavailable first mini-stack; the square depicts the acquired mini-stack; and the sparse rectangles represent the generated artificial interferograms between the compressed and the acquired SLCs. d) Third sequence: here, the artificial interferograms are generated with respect to the compressed SLCs of the first and the second mini-stacks. Estimated between the compressed SLCs and the mini-stack, the coherence of the artificial interferograms in (c) and (d) is an implication of the relation between the isolated mini-stacks. Indicated by this coherence, the quality of the artificial interferogram is evaluated adaptive to the data content of the mini-stack. Exploitation of the artificial interferograms while incorporating their coherence renders the data adaptability of the Sequential Estimator.

complement of the subspace spanned by \mathbf{v}_{ML} . The projection matrix corresponding to \mathbf{v}_{ML} reads as

$$C_{\text{ML}} = \mathbf{v}_{\text{ML}} \mathbf{v}_{\text{ML}}^H \quad (9)$$

and its orthogonal complement C_{ML}^\perp as

$$C_{\text{ML}}^\perp \oplus C_{\text{ML}} = I. \quad (10)$$

Note that C_{ML} and consequently C_{ML}^\perp are projection matrices, and I is the identity matrix. The coherence matrix can therefore be propagated via the orthogonal complement as

$$C_{\text{proj}} = C_{\text{ML}}^\perp C^n C_{\text{ML}}^\perp. \quad (11)$$

C_{proj} corresponds to the coherence matrix of the projected data to the residual subspace, after elimination of the ML component. The eigen decomposition of this coherence matrix provides the complementary vectors of the sought orthonormal basis

$$C_{\text{proj}} = \sum_{p=1}^{n-1} \lambda_p \mathbf{v}_p \mathbf{v}_p^H \quad (12)$$

and the transformation matrix of (5) is redefined by the resulted components, that is

$$T = \{\mathbf{v}_{\text{ML}}; \mathbf{v}_1; \dots; \mathbf{v}_{m-1}\}. \quad (13)$$

The data is compressed by its transformation to the range space of the defined T

$$\tilde{Z} = T^H Z. \quad (14)$$

As desired, the transformation projects the n -dimensional data in Z to the m -dimensional subspace represented by T , thus compressing the data volume. \tilde{Z} contains the m sorted compressed SLCs in its rows, such that the first row corresponds to the most coherent signal component. The first compressed SLC is given by

$$\begin{aligned} \tilde{z}_{\text{ML}} &= T_1^H Z \\ &= \mathbf{v}_{\text{ML}}^H Z. \end{aligned} \quad (15)$$

Expanding the above matrix product, it can easily be shown that the above formulation is equivalent to the coherent filtering of (3).

The introduced data reduction is the core method for information preservation in the Sequential Estimator, as it will be introduced in Section IV.

IV. SEQUENTIAL ESTIMATOR

The proposed Sequential Estimator pursues an efficient stacking scheme (see Section I for the defined criteria). The algorithmic efficiency criterion is imposed by processing the stack in isolated small batches, as schematically depicted in Fig. 1(a). To meet the requirement for the estimation efficiency, the scheme retrieves the coherent signal among the isolated batches. As it will be discussed in Section VI-C, neglecting even low-coherent interferometric pairs in the stack degrades the estimation performance.

Inspired by De Zan and López-Dekker [18], the Sequential Estimator is established based on the idea of retrieving the coherent signal without having full access to the data archive. The backbone of the method is using data compression and retrieving the coherence via formation of *artificial* interferograms between the compressed and the newly acquired data. The inclusion of the artificial interferograms enables the performance preservation.

The estimator is essentially a recursive algorithm with a link to the products of the prior steps at each sequence. For the sake of clarity, the recursion of the established method is shown schematically in Fig. 1 and algorithmically in Table I. The flowchart of the estimator at each sequence is given in Fig. 2. A brief synopsis of the scheme is provided below. Each single module of Fig. 2 is further elaborated in the sections.

With reference to Table I, the Sequential Estimator starts with the acquisition of a small chunk of s SLCs of the data stream, where $s \ll n$. The data is collected and processed in sequences, hence the name *sequential*. The data chunk is hereafter referred to as a *mini-stack*. The mini-stack undergoes

TABLE I

HIGH-LEVEL PSEUDOCODE DESCRIBING THE RECURSIVE NATURE OF THE SEQUENTIAL ESTIMATOR; EACH MENTIONED BLOCK IS COMPRISED OF DIFFERENT MODULES EXPRESSED IN FIG. 2; NOTE THAT ONLY SOME MODULES ARE RELEVANT TO THE INITIAL SEQUENCE

Initiation:	
Let $k = 1$ as an index of the sequence;	
Form Input Data Block :	
Perform: Acquisition of the first mini-stack	$\rightarrow Z_s^1$;
From Phase Estimation Block :	
Perform: Phase-linking	$\rightarrow \hat{\phi}^1$;
Perform Data Compression Block :	$\rightarrow \bar{Z}^1$;
Perform Data Archiving Block .	
While there is a new SLC acquisition:	
Wait until s SLCs are stored;	
Form a mini-stack from the s SLCs;	
Let $k = k + 1$ as an index of the sequence;	
Perform Input Data Block	$\rightarrow \bar{Z}^i \forall i \in [1, k-1], Z_s^k,$
Perform Data Augmentation Block	$\rightarrow \bar{Z}^k,$
Perform Phase Estimation Block	$\rightarrow \hat{\phi}^k,$
Perform Data Compression Block	$\rightarrow \bar{Z}^k,$
Perform Data Archive Block ;	
End	

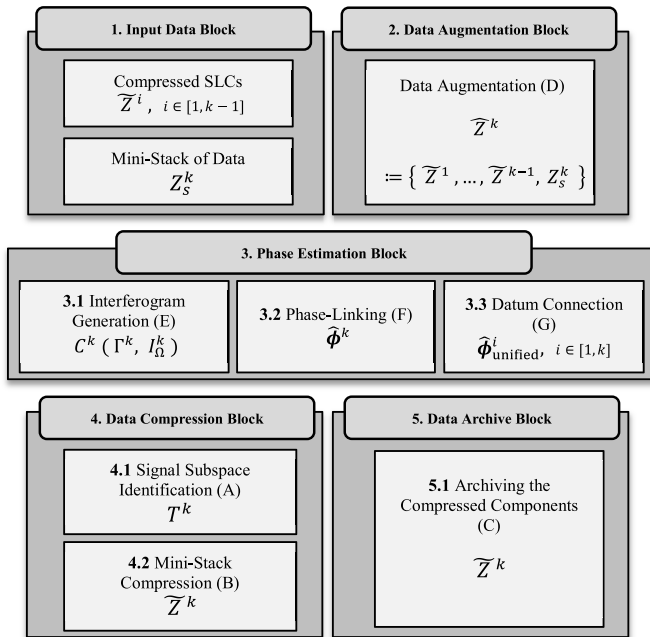


Fig. 2. Algorithmic flow of the Sequential Estimator at its k th sequence: each module is accompanied by its final product; superscripts correspond to the index of the sequence with i referring to the entire history prior to the current sequence. The specified letters in parenthesis correspond to the section in which the module is elaborated.

a two-step process: signal estimation and data compression. In the signal estimation step, the phase of each SLC in the mini-stack is estimated via MLE. In the data compression step, the SLCs are compressed by estimation of the underlying low-rank signal subspace and a further projection of the data to

this subspace. Processing of the first mini-stack concludes by archiving the compressed SLCs.

With reference to Fig. 2, at the subsequent mini-stacks, the same two-step phase estimation and data compression is pursued, although with minor changes. Prior to the phase estimation, the compressed SLCs are prepended to the current mini-stack. Exploiting the augmented data, artificial interferograms are generated between the acquired and the compressed SLCs. They in fact substitute the lost coherent signal among the isolated mini-stacks. The phase-linking includes the artificial interferograms and their corresponding coherence. In order to link the estimated phases of different sequences, a datum connection step follows. After the phase estimation block, the mini-stack is compressed and archived similar to the initial sequence.

The different processing modules are elaborated in the following. The sections follow a processing order starting from data compression of the first mini-stack in the initial sequence and ending at the phase estimation of its subsequent sequence.

A. Signal Subspace Identification

This module aims at finding the low-rank subspace for temporal compression of the mini-stack. The proposed orthonormal basis T of (13) is an optimum representative of this subspace, in case a linear transformation is desired. This section addresses the question of the optimum dimension of this subspace, i.e., the choice of m in (13).

As discussed in Section III, the complex coherence summarizes the information content of the SAR stack. The modulus of coherence matrix indicates the temporal decorrelation of the SAR signal. The temporal decorrelation arises from the position changes of the subresolution scatterers [27]. Random position changes impose a variation in the coherent mean of the scatterers. They are therefore reflected in both the modulus and the argument of the complex coherence. Systematic position changes of the subresolution scatterers, on the other hand, only impose a systematic phase shift in the mean scattering response. The latter effect is captured by a systematic phase term on the complex coherence rather than imposing a temporal decorrelation [27]. The systematic position changes are attributed, among other effects, to the surface motion, i.e., the geophysical signal. Therefore, although the coherence matrix is full rank, it mostly represents the decorrelation phenomenon. The geophysical signal is of much lower rank and spans a much lower dimensional subspace. MLE, in fact, estimates a rank-1 dyad as the first component of this low-rank subspace.

Assuming a single PS-resembling scattering, it suffices for the sequential scheme to include only the ML components of the subspace; by setting m to 1. Higher dimension of signal subspace is required in cases where the DS region exhibits multiple dominant systematic position changes along the elevation profile of the SAR 3-D resolution cell. The precise retrieval of such multiple geophysical signals falls in the realm of differential SAR tomography [28], [29]. Hereafter, a single dominant deformation signal is assumed and m is set to 1. Section VIII discusses the consequence of this simplification.

B. Mini-Stack Compression

The acquired SLCs in the mini-stack are compressed by projection of the data to the identified signal subspace following (14). For the sake of clarity, the compressed data is hereafter specified by accentuation with $\tilde{\cdot}$.

C. Data Archiving

\tilde{Z} is archived to be further exploited at the subsequent mini-stacks.

D. Data Augmentation

After the initial sequence, the data available to each further k th sequence is comprised of the following:

- 1) Z_s^k : the acquired s SLCs of the k th mini-stack;
- 2) \tilde{Z}^i : the compressed version of the i th mini-stack prior to the current one ($i = 1, \dots, k - 1$).

The compressed components are prepended to the acquired mini-stack, such that the augmented data \hat{Z}^k reads as

$$\hat{Z}^k = \left\{ \tilde{Z}^1; \dots; \tilde{Z}^{k-1}; Z_s^k \right\} \quad (16)$$

with $\hat{Z}^k \in \mathbb{C}^{(s+k-1) \times I}$. The augmentation is hereafter indicated by accentuation with $\hat{\cdot}$.

E. Interferogram Generation

At each sequence of processing, the coherent signal between the mini-stack and the unavailable data history is retrieved through generation of artificial interferograms, formed between each acquired SLC in Z_s^k and the compressed SLCs, that is

$$\left(\hat{I}_{\Omega}^k \right)_{ij} = \tilde{Z}^i \left(Z_s^k \right)_j^H \quad (17)$$

where the subscript indicates the j th row of the accompanied matrix.

The artificial interferograms are exploited jointly with the observed interferograms in the phase-linking. This joint exploitation prevents an expected performance loss for the batch-processing schemes.

F. Phase-Linking

At each sequence k , the phase-linking is carried out using the ML estimator of (2), that is

$$\hat{\phi}^k = \underset{\phi}{\operatorname{argmin}} \left\{ \hat{\xi}^H \left(\hat{\Gamma}^{k-1} \circ \hat{C}^k \right) \hat{\xi} \right\}. \quad (18)$$

Here, \hat{C}^k and $\hat{\Gamma}^k$ are estimated based on the augmented data \hat{Z}^k . Thus, they encapsulate both the observed and the artificial interferograms accompanied by their coherence, representing their statistics.

G. Datum Connection

The phase-linking formulated in (2) poses an under-determined problem [4], [5]. In multipass InSAR, this problem is tackled by constraining the phase of an arbitrary SLC, i.e., by setting this SLC as a datum in the time series and estimating the phase of the entire stack with respect to this datum. This solution is as well adopted in the Sequential Estimator, i.e., at each sequence the phases are estimated relative to one SLC in the augmented data. The problem with

this approach is that the estimated phases at each sequence are relative to their respective datum. The solution is to connect the defined datum of different sequences in order to provide a single fully connected phase series.

The datum connection can be achieved by performing a phase-linking on the \tilde{z}_{ML}^i components. Recall that these components represent their isolated mini-stacks. The interferometric phase between them therefore implies the datum separations. These phases are temporally integrated via a separate ML phase-linking; i.e., by treating the compressed SLCs as a new stack, generating the respective $\tilde{\Gamma}_{ML}$ and \tilde{C}_{ML} , and retrieving the phase of each sequence relative to a new arbitrary but unique datum via MLE

$$\hat{\phi}_{\text{cal}} = \underset{\phi}{\operatorname{argmin}} \left\{ \hat{\xi}^H \left(\tilde{\Gamma}_{ML}^{-1} \circ \tilde{C}_{ML} \right) \hat{\xi} \right\}. \quad (19)$$

$\hat{\phi}_{\text{cal}}$ is a vector containing the calibration phases that connects the isolated mini-stacks. The datum connection for the i th sequence is thus carried out

$$\hat{\phi}_{\text{Unified}}^i = \hat{\phi}^i + \hat{\phi}_{\text{cal}}(i). \quad (20)$$

Here, the superscripts identify the sequence, while $\hat{\phi}_{\text{cal}}(i)$ indicates the i th element of the calibration vector. Following this calibration step, a uni-datum phase time series results.

H. NRT Processing Capability of the Sequential Estimator

Up to this point, the proposed scheme awaits the acquisition of s images for formation of a mini-stack and only then starts the processing at each sequence. The scheme may be expanded within the mini-stack to accommodate the NRT processing of each acquired SLC. In other words, upon acquisition of each SLC within the mini-stack, we may allow the accustomed processing scheme via replacing the Z_s^k in (16) by the interim data chunk of less than s SLCs. The size of the interim data chunk increases from 1 to $s - 1$ SLCs and enables phase estimation of each SLC upon its acquisition. Note that the compressed data prior to the interim data chunk is still exploited in the phase-linking. In this fashion, the phase estimation is repeated within the mini-stack until s SLCs are acquired. The number of repetitions is, however, limited by the size of the mini-stack, rendering the increased computational burden bounded as opposed to the conventional full-stack processing approaches.

With reference to Fig. 2, only Blocks 1, 2, and 3 are relevant for NRT processing within the mini-stack. The data compression and archiving blocks are carried out only after the accumulation of the entire s SLCs of the mini-stack.

V. NOTE ON THE COMPUTATIONAL GAIN

In conventional MLE phase-linking, the computational time complexity is driven by the number of SLCs involved. The computational burden is primarily imposed by the iterative ML optimization for phase estimation and secondarily by the regularization and inversion of the complex coherence matrix. Trivially, both are affected by the number of interferograms.

Assuming a stack of n SLCs, $n(n-1)/2$ interferograms are generated and exploited in the phase-linking. Adopting the

sequential approach, the size of the available SLCs in the last mini-stack reduces to $(s^2 - s + n)/s$, the number of interferograms decreases accordingly.

Besides the reduced computational burden, the need for updating and re-estimation of the entire phase history at the face of each single acquisition is prevented by the sequential scheme. The scheme in fact enables efficient processing of an inherently nonparallel problem in the temporal domain. The reduction of the data volume, from the entire stack to the compressed SLCs is another gain of the algorithm regarding the data storage capacity.

As an example of the efficiency of the algorithm, let us take the expected seven-year life of Sentinel-1 mission. With the six-day revisit of the mission, a rough number of 400 SLCs may be expected for a region of interest. Conventional processing of such stacks requires the generation and exploitation of 79 800 interferograms. Adopting the Sequential Estimator with mini-stack size of 20, the number of SLCs reduces to 39 and the number of interferograms to 741 at the last mini-stack. However, it shall be mentioned that the cumulative number of interferograms of all mini-stacks prior to the last sequence sums up to 8740. However, in contrast to the full-stack schemes, the processing of this number of interferograms is spread over the acquisition time and is not imposed at once. In terms of storage capacity, the 400 SLCs may be replaced by 20 compressed SLCs.

Trivially, the processing gain of the Sequential Estimator is affected by the mini-stack size. The choice of an optimum mini-stack size requires further investigation. A separate yearly compression of the data might as well be considered to enhance the processing/archiving reduction factors; the corresponding estimation efficiency shall, however, be studied.

VI. PERFORMANCE ASSESSMENT WITH SIMULATIONS

For validation and performance evaluation purposes, the Sequential Estimator is tested and compared to the conventional phase-linking algorithms using simulated data.

Reflected in the coherence matrix, the maximum achievable precision is bound by signal decorrelation [6]. The impact of the decorrelation process on the performance of different approaches including the proposed estimator is investigated here.

A. Simulation Scenarios

The error source to be tackled by phase-linking is the temporal decorrelation. In order to investigate its impact, two models are considered here. The first is a purely exponential decorrelation between acquisition pairs, that is

$$\Gamma_{p,q} = \gamma_0 \exp\left(\frac{-t_{p,q}}{\tau_0}\right) \quad (21)$$

while the second reveals a residual coherence even for large temporal baselines, that is [23]

$$\Gamma_{p,q} = (\gamma_0 - \gamma_\infty) \exp\left(\frac{-t_{p,q}}{\tau_0}\right) + \gamma_\infty. \quad (22)$$

In these formulations, $\Gamma_{p,q}$ is, as usual, the coherence between the p th and q th SLC of the stack, γ_0 and γ_∞ indicate,

TABLE II
PERFORMANCE OF THE VARIOUS PHASE-LINKING SCHEMES COMPARED TO THE CRLB, USING 300 LOOKS IN COHERENCE ESTIMATION; REPORTED IS THE RMSE OF THE ESTIMATED PHASE FOR THE INTERFEROGRAM WITH LONGEST TEMPORAL BASELINE (600 DAYS). THE PROPOSED SEQUENTIAL ESTIMATOR PROVIDES A TRADE-OFF BETWEEN THE MLE AND StBAS

Coherence Scenario	Model	Exponential Decay	Long-Term Coherence
	Equation		21
Simulation Parameters		$\gamma_0 = 0.6$ $\tau_0 = 50$ days	$\gamma_0 = 0.6, \gamma_\infty = 0.2$ $\tau_0 = 27$ days
RMSE Phase Estimation [rad]	MLE	1.43	0.12
	EVD	1.54	0.12
	StBAS	0.29	0.21
	Virtual Ifgr. Est.	1.83	0.12
	Sequential Est.	0.55	0.11
	CRLB	0.28	0.10

respectively, the initial and residual coherence, $t_{p,q}$ stands for the temporal baseline, and τ_0 is the time constant of the decorrelation process. Note that for $\gamma_\infty = 0$ the two models are identical. The aforementioned scenarios manifest two extreme cases for any phase-linking scheme. In the exponential decay, the interferograms with large temporal baseline bear no coherent signal while in the long-term coherence, a possibly weak, coherent signal is present regardless of the temporal separation of the SLCs.

Based on the temporal models, two coherence matrices are simulated corresponding to the exponential decay and long-term coherence. Given the simulated coherence matrices, two stacks of 100 SLCs, each containing an ensemble of 300 statistically homogeneous samples, are synthesized as follows.

- 1) The CCG statistic and spatial stationarity are assumed in the generation of the data stack.
- 2) The topographic, atmospheric, and deformation phase is set to zero.
- 3) The temporal sampling interval, similar to Sentinel-1, is set to six days.

The decorrelation model parameters of the simulated stacks are provided in Table II.

The simulated coherence matrix and its estimation using the synthesized stack are depicted in Fig. 3. Comparing the estimated and simulated coherence matrices, the well-known error of coherence estimation is observable [7], [8]. The performance of coherence estimation is governed by the size of ensemble used in the estimation as well as the coherence level [7], [8]. It is degraded for coherences close to zero and may be improved by exploiting a larger Ω neighborhood. However, the increase in the size of Ω shall be dealt carefully as it can compromise the spatial stationarity of the ensemble.

In practice, the positive definiteness of the estimated coherence is not guaranteed. In such cases, the coherence matrix is regularized via diagonal loading, i.e., the addition of small fraction to the diagonal elements of the coherence

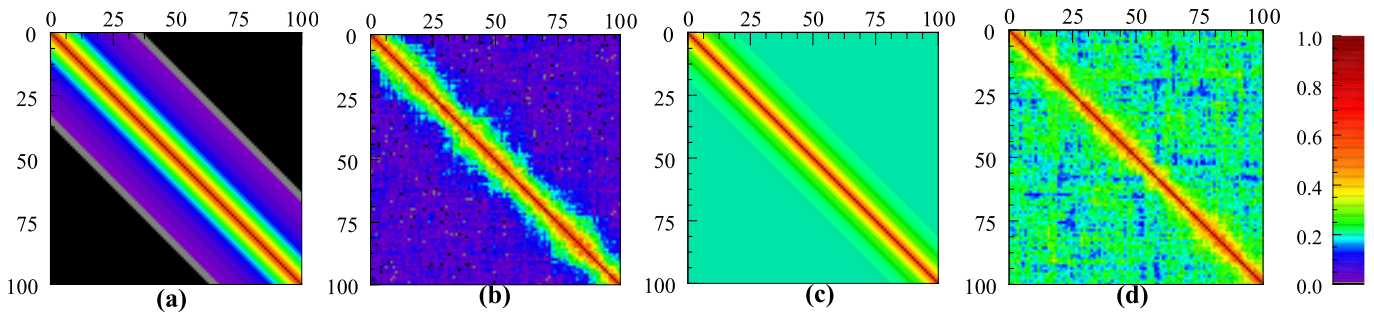


Fig. 3. Coherence matrix of the two considered simulation models; (a) and (b) fast exponential decay and (c) and (d) long-term coherence model; (a) and (c) simulated (true) coherence; (b) and (d) estimation of the coherence using the simulated CCG ensemble with 300 looks; the color scale is identical for all matrices; and the well-known coherence estimation error is observable and is more pronounced for lower coherence level. Increasing the number of samples, the performance of coherence estimation improves and the estimated coherence asymptotically approaches its true values.

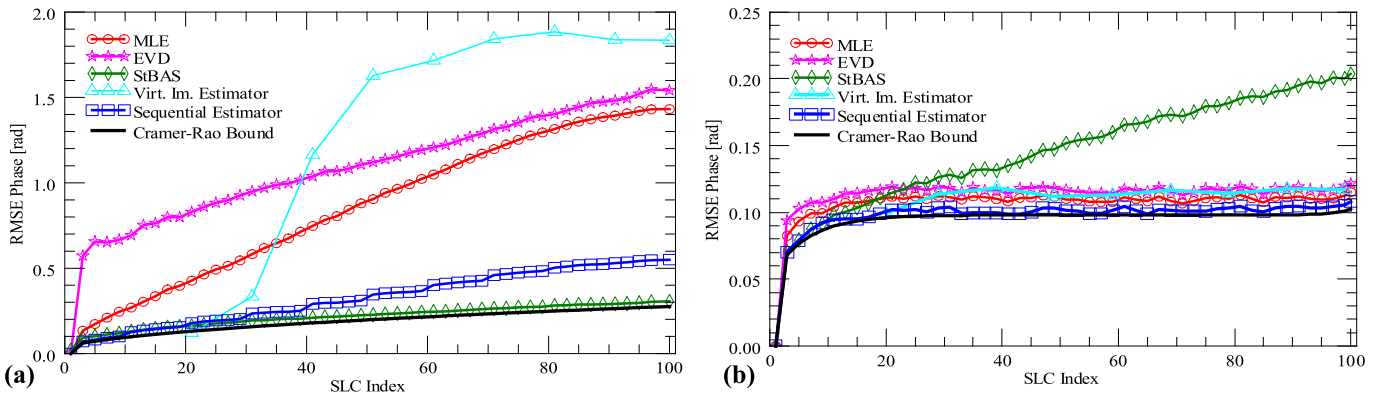


Fig. 4. RMSE of phase estimation as the performance indicator of the Sequential Estimator compared to the MLE, EVD, StBAS, virtual image estimator, and the CRLB; considering (a) Fast exponential decaying coherence and (b) Long-term coherence scenario. The StBAS is the optimum solution in case of fast coherence loss while MLE outperforms it when a weak but long-term coherent signal is present. Evidently, the optimality of the mentioned estimators depends on the coherence scenario. In both cases, the Sequential Estimator retains a balanced performance close to the CRLB, proving to be a generic solution and adaptable to the coherence scenario [note the different scale of (a) and (b)].

matrix (see [11]). This operation iteratively increases the negative eigenvalues of the coherence matrix, thus ensures the positive definiteness of the regularized coherence and consequently its inverse.

B. Comparison Scenarios

The objective is to compare different phase-linking techniques. The following estimators with their specified details are considered.

- 1) *MLE*: Using the iterative solution proposed in [4].
- 2) *EVD*: Exploiting the dominant scattering mechanism corresponding to the largest principal component.
- 3) *StBAS*: phase-linking exploiting the short temporal-baseline interferograms with baseline of up to 60 days. It is equivalent to accessing up to lag-10 SLCs at each processing level.
- 4) *Virtual Image Estimator*: Using two subsets of 10 SLCs, the first is fixed at the beginning of the stack, the second coincides with the Sequential Estimator's mini-stacks;
- 5) *Proposed Sequential Estimator*: Accessing isolated mini-stacks of 10 SLCs and setting $m = 1$;
- 6) *Cramér–Rao Lower Bound*: The theoretical, i.e., simulated coherence is exploited for the calculation of the CRLB.

C. Performance Assessment

The root-mean-square error (RMSE) of the estimated with respect to the simulated phases is considered for the performance assessment. This measure encapsulates both the bias and precision of the corresponding estimator.

Using 1000 realizations, the RMSE of the two defined simulation scenarios is calculated. Table II summarizes the simulation cases as well as the RMSE of the estimated phase of the last SLC in the simulated stacks.

Fig. 4(a) and (b) depicts the performance of different estimators for the exponential decorrelation and long-term coherence scenarios, respectively. Note that the CRLB is calculated with the theoretical coherence given by (21) and (22), while the different estimators use the estimation of the coherence according to (1).

Comparing Fig. 4(a) with Fig. 4(b) reveals the influence of the decorrelation mechanism on the performance of the estimators. Even a weak signal, with coherence as low as 0.2, improves the precision of ML phase estimation by a factor of ~ 12 . This observation emphasizes the importance of the inclusion of even low-coherent interferograms in *phase-linking*. As explained in Section III, it is further noticeable that the EVD asymptotically approximates the MLE in both cases. The behavior of the virtual image estimator in the

two different cases is also worthy of notice. As expected, the phase estimation is compromised in the absence of a coherent signal between the two subsets; i.e., beyond the correlation length of the exponential signal in Fig. 4(a) (~ 210 days).

Inspecting Fig. 4(a), StBAS outperforms other approaches by having the closest performance to the CRLB. Theoretically, however, the MLE is expected to be the closest to the bound. The odd behavior of MLE lies in the suboptimality of the coherence estimation (see Fig. 3). It may in fact be shown that substituting the simulated, i.e., true, coherence, the MLE attains its asymptotic performance to CRLB. The coherence estimator performs poorer for coherence levels close to zero, as is the case for the majority of interferograms in the current simulation. Exploiting such suboptimum coherence matrix, the MLE is misled toward relying on the pure noise-bearing interferograms in its estimation of the phase series. However, the StBAS naively ignores interferograms with temporal baselines of larger than 60 days and merely exploits the high-coherent interferograms for which the coherence estimation is known to perform better. The latter is therefore immune to the coherence error. Comparing the different estimators, all schemes based on the full exploitation of the coherence matrix are compromised by the coherence error. This impact is also conveyed by an independent study in [10]. Coming to the proposed Sequential Estimator, the performance loss is not as dramatic as the full-stack-exploiting schemes. The performance preservation may be explained by the exploited data compression in the Sequential Estimator. Recall that the noise components of the data space are suppressed in the data compression. The artificial interferograms between the mini-stacks are therefore less affected by the noisy interferograms and in general of higher SNR compared to the respective initial SLCs. This intermediary filtering of the mini-stacks enhances the performance of the Sequential Estimator compared to the MLE or EVD.

The impact of coherence estimation on the performance of MLE highlights the importance of the considered stochastic model in the phase-linking scheme. Although this issue is beyond the scope of this contribution, we briefly discuss the potential solutions and leave further investigations to future works. The improvement of the coherence estimation [7], [30] or modification of the stochastic model is two possible ways to approach the problem. Regarding the latter, the robust estimation schemes, e.g., the robust M-estimator of [11], may be adopted to modify the stochastic model relative to *a posteriori* residuals. While the MLE relies solely on the inverse of the coherence matrix and is misled by its poor estimation, the robust scheme adaptively down weights the outlying noise-bearing interferograms, hence balances the role of the coherence as the only weighting criterion in the MLE.

Examining the long-term coherence scenario in Fig. 4(b) reveals a contrasting behavior of the estimators compared to the exponential decay. Having exploited the long-term coherence, the full-stack-exploiting schemes outperform StBAS in this scenario. The performance of StBAS deviates from the CRLB. This degradation is due to discarding the low-coherent interferograms with $\gamma_\infty = 0.2$. This observation corroborates the importance of inclusion of even low-coherent (but nonzero)

interferometric pairs in phase-linking. Retrieving the long-term coherent signal among the mini-stacks via artificial interferogram, the Sequential Estimator maintains its performance close to the CRLB.

Coming back to the comparison of these two coherence scenarios, different stacking strategies are observed to be suited to each case. The proposed Sequential Estimator is, however, shown to provide a balance between the two alternative schemes as it retains performance close to the CRLB in both scenarios. It may therefore be proposed as a generic approach, adaptive to the coherence pattern.

VII. EXPERIMENTS WITH REAL DATA

A time series of Sentinel-1 data is chosen for the first demonstration of the Sequential Estimator. A test site is picked in the southern volcanic islands of Italy known as Salina. Fig. 5 is an optical view of the Salina Island revealing the variety of land cover in the scene, ranging from rocky areas as probable PSs to sparse vegetation as possible DS regions. Data sets in interferometric wide-swath mode are obtained for this test site. The acquisitions were taken from December 2014 to April 2016 from a descending orbit, providing 38 SLCs. Fig. 6(a) and (b) shows the coherence of the observed interferograms with the shortest and longest temporal baselines, revealing the interferometric quality of the data set. As apparent, the data stack undergoes severe decorrelation, rendering the phase-linking a necessary but challenging task for this data stack. Fig. 6(c) depicts the observed interferogram pertaining to the longest temporal baseline of 564 days. This interferogram is estimated via spatial adaptive filtering. In fact, the phase-linking schemes further perform a temporal filtering that improves the estimation of this interferogram, as it will be shown later in this section.

The aim here is to estimate the wrapped phase series, inclusive of the geophysical and atmospheric signals, via phase-linking. The separation of the atmosphere from the geophysical signal follows from a second processing step as in the case of PSs [1], [2]. This step is common to all DS schemes, thus of no interest for the current demonstration of the Sequential Estimator.

Setting $s = 10$, the Sequential Estimator divides the data set into four isolated mini-stacks; the last mini-stack contains eight SLCs. The phase estimation is performed on full spatial resolution. The pointwise complex coherence matrices are, however, estimated based on an ensemble of pixels in the homogenous Ω region surrounding each pixel. The Ω is found using Anderson–Darling statistical similarity test on the amplitude data [31]. The false alarm rate, a.k.a. the p -value, of the test is set to 5%. Note that the detection of Ω is merely based on the first mini-stack. Such a chosen homogeneous region is further utilized for the future mini-stacks. To improve the spatial stationarity in the homogeneous region, the topographic-induced phase is simulated using the Shuttle Radar Topography Mission digital elevation model and reduced from the SLCs prior to the coherence estimation. At each mini-stack, the data is compressed by fixing m to 1; using \tilde{z}_{ML} compressed SLCs only. The data volume is thus compressed by 90 percent.

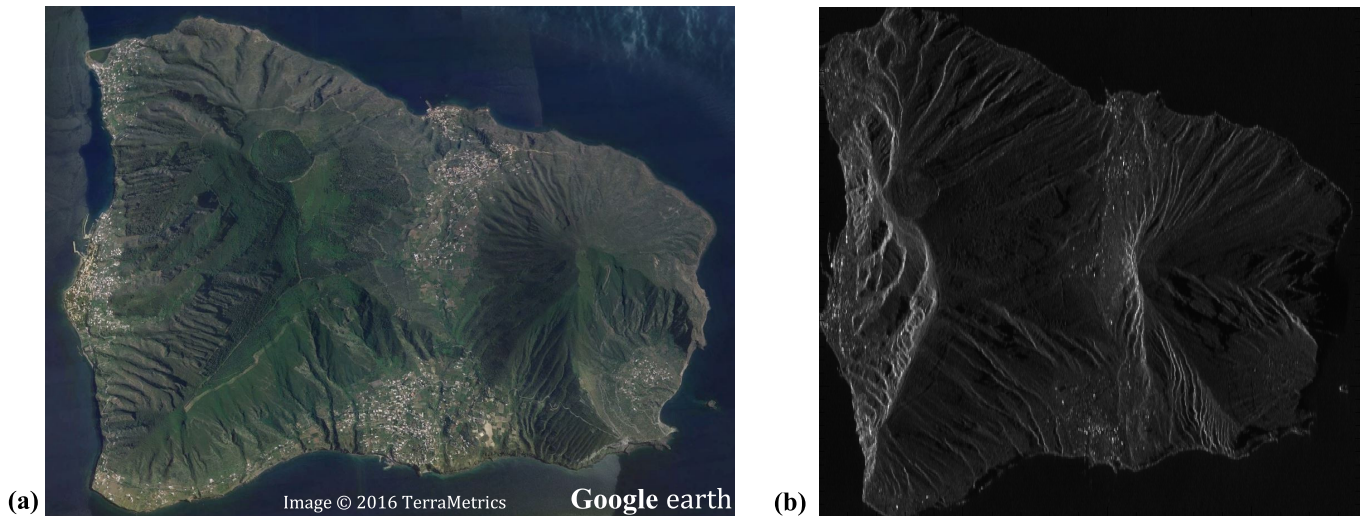


Fig. 5. View of the Salina Island located in Southern Italy. (a) Optical image from Google Earth showing the various land covers of the chosen test site. (b) Temporally averaged amplitude map of the test site estimated from 38 SLCs of the Sentinel-1 SAR data stack.

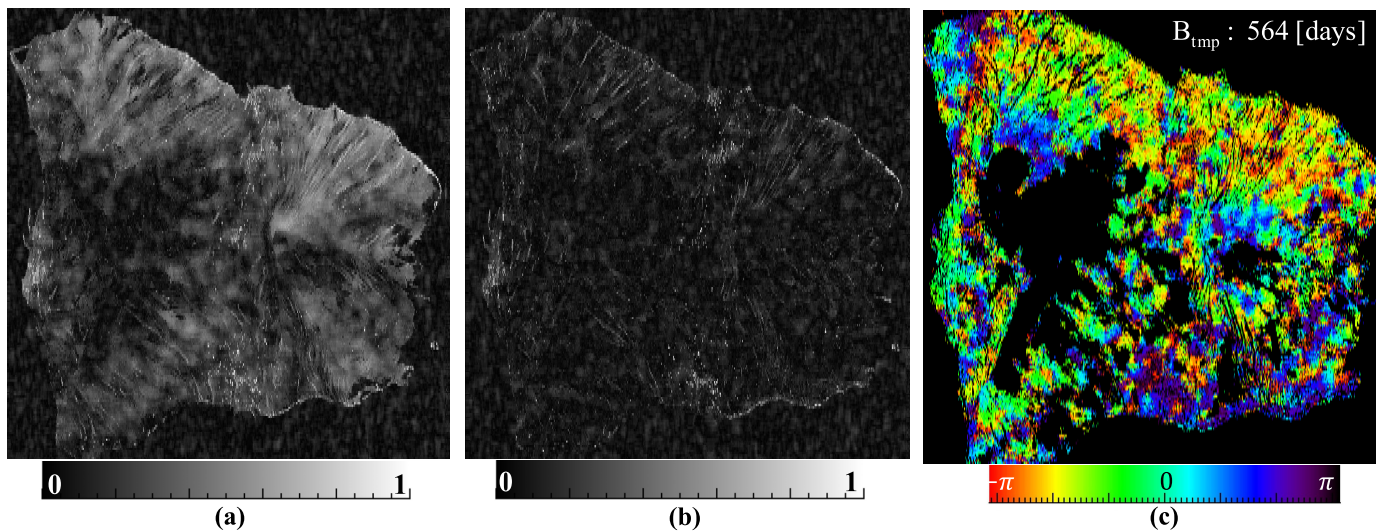


Fig. 6. Interferometric content of the Salina data stack; coherence of the observed interferograms with temporal baseline of: (a) 12 days and (b) 564 days, and (c) adaptive-multilooked observed interferogram of the latter. The coherence map of the long temporal-baseline interferogram indicates the severity of the temporal decorrelation. phase-linking provides an estimate of this interferogram by overcoming the temporal decorrelation (see Fig. 9).

In order to analyze the performance of the Sequential Estimator, MLE phase-linking is independently performed on the full stack. The result is used as a benchmark for comparison. The implementation details of the MLE are kept similar to the phase-linking of each mini-stack, the only difference being the detection of the homogeneous pixels in Ω for coherence estimation. The performance of the latter detection is driven by the stack size [20] as well as the p -value set for the hypothesis testing [31]. Fixing the p -value, the similarity test for the MLE is performed on the full data stack of 38 SLCs, hence with higher precision compared to the Sequential Estimator, where a mini-stack of 10 SLCs is used [20]. Fig. 7 reveals the sensitivity of the test result to the stack size by providing the size of the detected ensemble surrounding each pixel. Note that exploiting a single mini-stack, the number of similar pixels is overestimated, possibly introducing outliers in coherence estimation. One approach to tackle this problem is to adjust

the p -values of the hypothesis testing, i.e., decreasing it to lower the probability of inclusion of less similar samples. Two alternative approaches are proposed in [32] and [33]. As it will be revealed in the comparison results, even with a poor DS detection, the Sequential Estimator achieves a performance close to the MLE. It should be noted that the homogeneity of the Ω neighborhood may be disturbed by some or all pixels, after its detection in the first mini-stack. This issue is subject to future studies and algorithmic enhancement to sequentialize the DS detection as well.

In the following, different strategies are considered to compare the performance of Sequential Estimator versus the full-stack MLE phase-linking.

A. Posteriori Coherence of the Phase Series

Proposed by Ferretti *et al.* [5], the quality of the phase-linking may be assessed by the goodness of fit between the

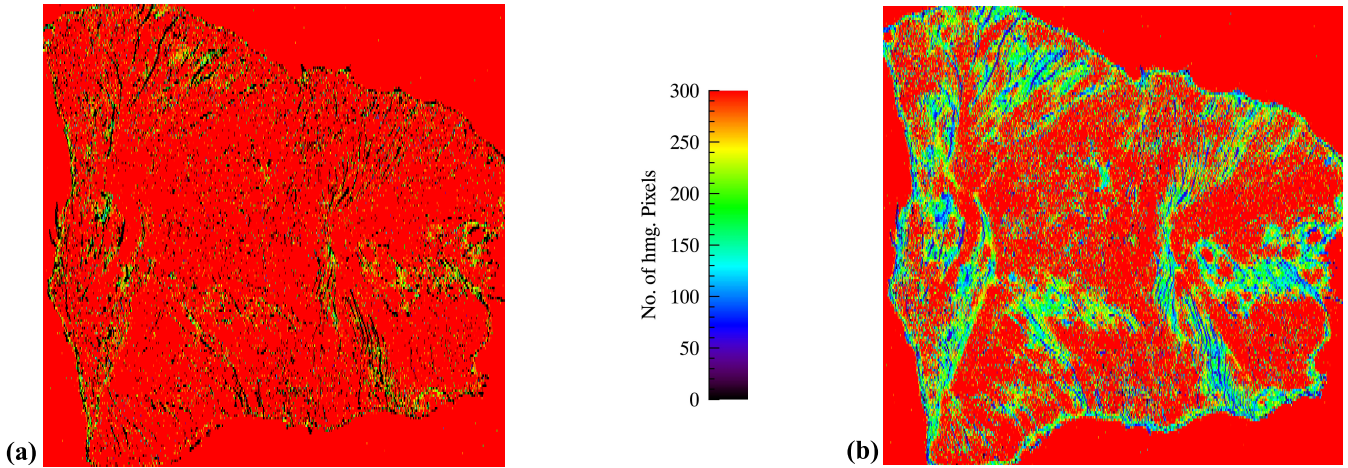


Fig. 7. Number of detected statistically homogeneous samples surrounding each single pixel, as a result of the Anderson–Darling similarity test, under the fixed p -value of 5%, by (a) exploiting 10 SLCs of the first mini-stack as in the Sequential Estimator and (b) using all 38 SLCs of the stack as in the full-stack MLE scheme. As expected, the detection rate is governed by the number of exploited SLCs.

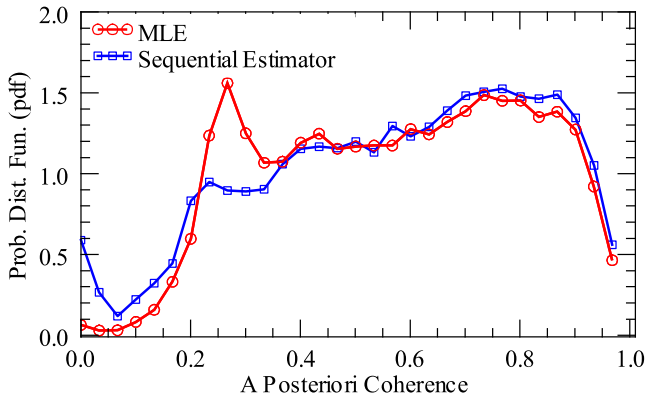


Fig. 8. *A posteriori* coherence as the quality measure of the Sequential Estimator and the full-stack MLE; the Sequential Estimator slightly enhances the phase-linking; and note that the quality measure is highly biased at low coherence pertaining to water and dense vegetation land cover especially in the case of MLE.

estimated and the observed phases, that is

$$\hat{\gamma} = \frac{\text{Re} \left\{ \sum_{q=1}^n \sum_{p=q+1}^n e^{j(\Delta\phi_{pq} - (\hat{\phi}_p - \hat{\phi}_q))} \right\}}{n(n-1)/2} \quad (23)$$

with $\Delta\phi_{pq}$ as the observed interferometric phase between p and q SLCs. Referred to hereafter as the *a posteriori* coherence, this quality measure reflects the validity of the assumed PS-resembling model for the approximation of the DS scattering behavior.

Fig. 8 shows the probability distribution function (pdf) of the *a posteriori* coherence of the entire scene for both the Sequential Estimator and the MLE. Comparing the two hint a slight improvement of Sequential Estimator over the MLE. The pronounced mode of the MLE's pdf at $0.2 < \hat{\gamma} < 0.3$ is a feature worthy of further examination: spatial investigations reveal that the mode pertains to water and dense vegetation land cover, where fast decorrelation is expected. In such cases, the MLE yields an overestimation of the quality measure, while the Sequential Estimator justifiably estimates the measure closer to zero; prompting the local mode of the latter's pdf at zero. This observation implies that although the *a posteriori* measure provides a good approximation at

high coherence values, it overestimates the quality at low coherences ($\sim \hat{\gamma} < 0.5$). This implication is positively verified via simulations.

The *a posteriori* coherence is hereafter used for filtering the result and performance assessment; however, its bias shall, be noted in the interpretation of the performed comparisons.

B. Spatial Inspection of the Estimated Interferograms

Having the wrapped phase series, an estimation of the interferograms is provided by the pairwise differential phases. The spatial inspection of such interferograms highlights the merit of the temporal filtering performed by the phase-linking. As expected, the longer the temporal baseline, the more severe is the temporal decorrelation. The examination of the estimated long-baseline interferograms is therefore more conclusive for the examination of the quality of the temporal filtering. Bearing this in mind, among all possible interferometric pairs, the one with the largest temporal baseline of 564 days is chosen to be presented here (Fig. 9). The estimated interferogram from the MLE and Sequential Estimator phase series are visually identical; therefore, the discrepancy between the two estimators is presented in Fig. 9(c) instead. To prove the efficiency of the sequential scheme, the estimated interferograms from StBAS phase-linking is demonstrated as well [Fig. 9(a)]. Note that only the consecutive, i.e., lag-1, SLC combinations are exploited in StBAS. As a visual assessment of the performed temporal filtering, the estimated interferograms of Fig. 9 may be compared to the corresponding observed interferogram in Fig. 6(c).

Comparing the estimated interferograms, the Sequential Estimator is shown to efficiently estimate a spatially smooth signal, and keep a close performance to the MLE, while the StBAS is severely degraded. This result once again emphasizes the importance of strategic efficient phase estimation as opposed to naive negligence of long-term interferograms.

C. Spatiotemporal Assessment of the Phase-Linking

Taking MLE as the reference, the focus here is on the quantitative performance analysis of the Sequential Estimator

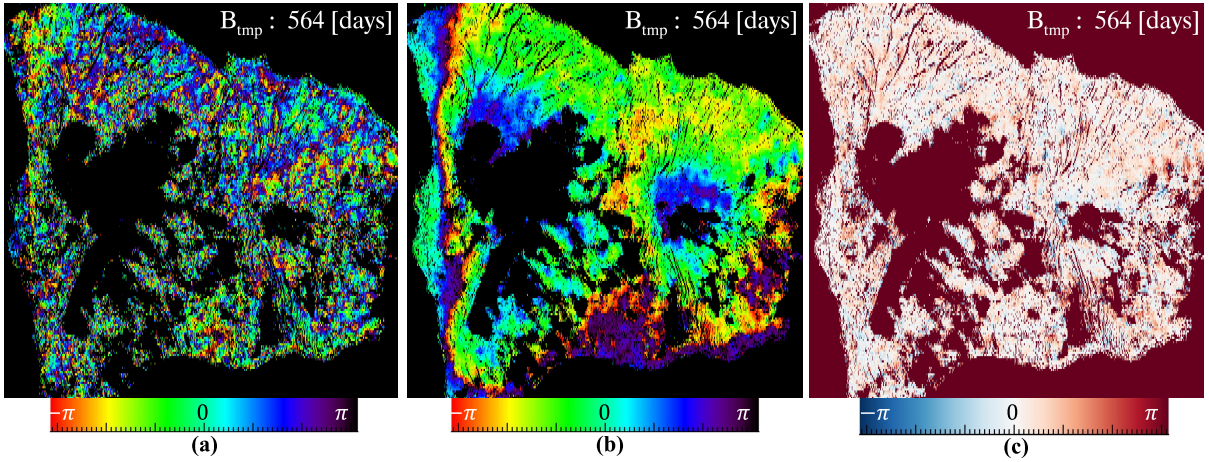


Fig. 9. Spatial inspection of the estimated interferograms with the longest temporal baseline of 564 days: (a) using StBAS by exploitation of the consecutive SLCs, (b) applying the Sequential Estimator, and (c) discrepancy between the Sequential Estimator and the full-stack MLE. The Sequential Estimator retains a performance close to the MLE and thus asymptotically to CRLB. Using the lag-1 interferograms, StBAS ignores the redundant interferograms and therefore fails in temporal filtering. The corresponding observed interferogram is provided in Fig. 6(c).

with respect to the MLE. The performance is evaluated by the discrepancy between the estimated phase series of the two mentioned schemes. Having performed phase-linking in a pixel-wise fashion, the phase discrepancies consist of $r_{rg} \times r_{az}$ values in the spatial and $n-1$ in the temporal direction. To have a statistical analysis on the performance, the $r_{rg} \times r_{az} \times (n-1)$ phase discrepancy values are accumulated. Exploiting the spatiotemporally accumulated discrepancies, the histogram of the inconsistency between the two methods is evaluated in Fig. 10; for visualization purposes the histogram is normalized by its maximum.

It shall be noted that the estimation results contain the noisy phases of the surrounding water of the island. The *a posteriori* coherence is used to mask such pixels. The coherence threshold is set to $\hat{\gamma} \leq 0.4$; same mask is used for the visualization of the interferograms in Figs. 6 and 9.

As apparent from these figures, the surrounding water as well as part of the caldera is concealed by the introduced mask. Inspecting the optical view of the island, the latter corresponds to denser vegetated area, where the approximation of DS region by PS-resembling model fails, hence compromise of the estimated *a posteriori* coherence value.

Fig. 10 depicts the histogram of the accumulated phase discrepancies for both original and masked estimation results. The Sequential Estimator is in agreement with the full-stack MLE, as evident from the first and second moments. These measures indicate the bias and the precision of the Sequential Estimator with respect to the MLE. Given Sentinel-1's 5.405 GHz sensor frequency at C-band, the estimated bias and precision of 0.1 and 0.52 rad translate to 0.44 and 2.2 mm in slant range, respectively. The reported performance is prior to the separation of the atmospheric signal.

D. Performance With Respect to the *a Posteriori* Coherence

Described in the previous section, the spatiotemporal accumulation of the phase discrepancies is exploited here as well. The normalized histogram of phase discrepancies corresponding to different *a posteriori* coherence levels is evaluated in Fig. 11; providing the estimation bias and

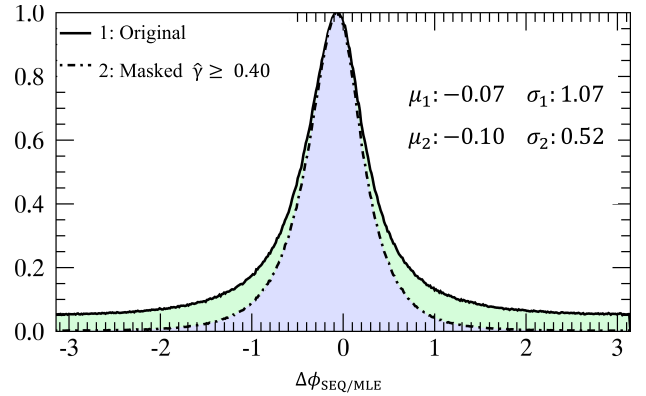


Fig. 10. Spatiotemporal analysis through normalized histogram of the phase discrepancy between the MLE and Sequential Estimator; the overall performance of the Sequential Estimator relative to the MLE is resulted from the histograms (see Section VII-C for details on the utilized mask).

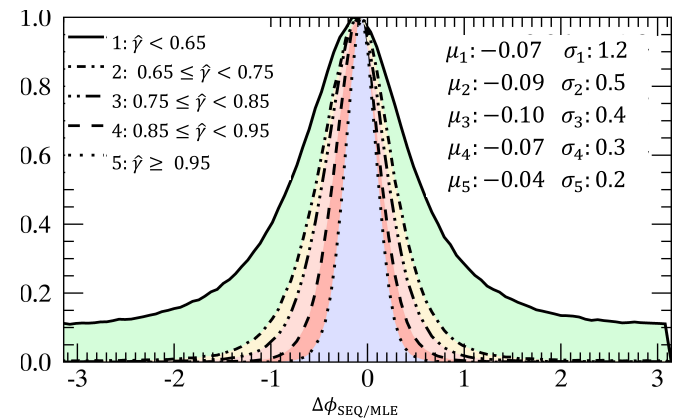


Fig. 11. Performance of the Sequential Estimator at different coherence levels compared to the MLE; the bias (μ_i) and precision (σ_i) of the estimator is reported relative to the *a posteriori* coherence, with i referring to the reported coherence level. The agreement between the two methods increases with the increase of the coherence.

precision of the Sequential Estimator relative to the quality of phase-linking. As revealed from the simulations of Section VI-C, in the case of higher coherence, the performance of the two estimators is closer than cases of fast decorrelation.

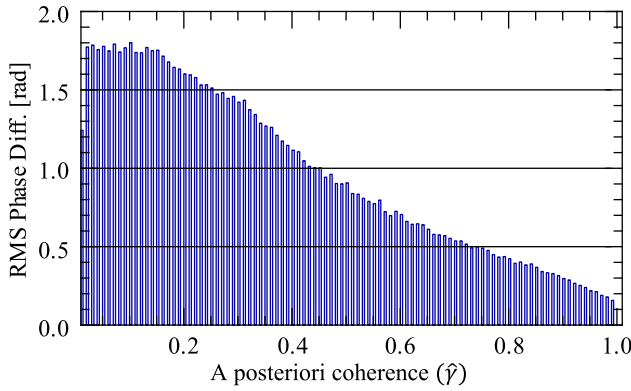


Fig. 12. RMS of the phase discrepancies between the Sequential Estimator and the MLE; the agreement of the two methods increases with the *a posteriori* coherence. The high difference at low coherences may stem from the poor performance of the MLE. An independent validation with PSI or GNSS, therefore, provides a more conclusive approach at low coherences.

In the pursuit of retrieval of the geophysical parameters, it is common practice to discard low quality estimated phases in the processing steps to follow. Considering such masking and choosing a coherence threshold of 0.85, the bias and precision of the Sequential Estimator improves to 0.07 and 0.3 rad equivalent to 0.3 and 1.3 mm in slant range, respectively.

E. RMS With Respect to the MLE

As the final assessment strategy, the accumulated phase discrepancies are grouped according to their *a posteriori* coherence in regular coherence intervals. The root mean square (RMS) of the discrepancies at each ensemble is further evaluated, providing the discrete phase difference as a function of the *a posteriori* coherence in Fig. 12. As depicted, the difference measure is governed by the coherence. At high coherence, the agreement of the two schemes is evident. At low coherence levels, however, the comparison is not as straightforward. As observed in Section VI-C, the MLE is severely erroneous in fast decorrelation scenarios. The high RMS values at low coherence levels may therefore stem from poor performance of the MLE. A more conclusive comparison shall be considered for the performance assessment specifically at low coherence. We suggest validation with independent InSAR or geodetic techniques, such as Persistent Scatterer Interferometry or Global Navigation Satellite System, as decisive approaches. For the sake of consistency, such validations are postponed to separate investigations.

VIII. CONCLUSION

The Sequential Estimator is proposed as an efficient processing scheme to exploit the unprecedented Big Data in InSAR. The main objective of the estimator is to move toward an NRT processing scheme while retaining the optimality of phase estimation close to the CRLB. The latter objective accommodates high-precision monitoring of small-scale earth surface deformations.

Performing comparisons with conventional stacking approaches, the role of coherence estimation is highlighted as the major obstacle for achieving high-precision phase

estimation. Supported by the simulation studies in this paper, the proposed Sequential Estimator is shown to reduce the impact of coherence estimation error owing to its intermediate filtering of the interferograms at each sequence. However, this potential of the estimator for improving the phase-linking shall be studied via independent validation, e.g., with GNSS or PSI techniques, and is not proven as of present.

The proposed scheme suggests a generic guideline for efficient processing of large data stacks via recursive estimation of the complex covariance for the InSAR stacks. The core elements are data compression and the generation of the artificial interferograms. The implementation steps for fulfilling the core tasks, e.g., phase-linking and data compression techniques may be replaced by a wide range of alternative solutions and may therefore improve the algorithmic and/or estimation efficiency of the Sequential Estimator. The following are instances of such improvements which give direction for future investigations:

The current proposal for implementation of the Sequential Estimator simplifies data compression by setting the dimension of the signal subspace to 1. According to the experiments with real-data higher order components do not have a contribution in the performance of the estimator. Theoretically, however, this simplification might trouble the Sequential Estimator in two scenarios: 1) in the presence of more than one dominant systematic change in the resolution cell and 2) in extreme exponential decaying coherence scenarios where the DS undergoes total decorrelation at a pace much faster than the sampling rate of the Sequential Estimator, governed by the mini-stack size. Apart from increasing m , the latter may be solved by adapting the size of the mini-stack or considering overlap between the mini-stacks. Therefore, two directions for future research are: 1) the generalization of the Sequential Estimator for $m > 1$, such that its response to generic coherence scenarios is not compromised (see [9] for an instance of such generalization) and 2) further studies on the choice and possible adaptability of mini-stack size.

Having the MLE as its phase-linking approach, the performance of the Sequential Estimator at each sequence is bound to the performance of the MLE and especially its sensitivity to the coherence estimation. Any improvement of the MLE and/or the coherence estimation therefore enhances the Sequential Estimator.

The core MLE may be replaced by more agile, but sub-optimum, phase-linking schemes. Examples are SBAS-like approaches, EVD or the like, which potentially reduce the computational burden of phase-linking within the mini-stack. Such simplification compromises the sensitivity to the small-scale geophysical signals and is thus only allowed dependent on the permissible performance degradation.

The PCA approach for data compression is primarily chosen due to its algorithmic efficiency. This simple approach may be substituted by more rigorous low-rank approximation schemes, with examples ranging from projection pursuit and independent component analysis to robust PCA. The drawback is, however, the increase in the computational burden.

A future research direction in the realm of sequential processing is the introduction of sequential statistical similarity

tests. The latter shall address possible changes to the homogeneity of the defined DS neighborhood which might occur after its detection in the first mini-stack. Such improvements may as well improve the detection of homogeneous ensembles for coherence estimation.

ACKNOWLEDGMENT

The authors would like to thank colleagues from the German Aerospace Center (DLR): Dr. R. Shau for the preparation of Sentinel-1 Data, Dr. K. Goel for provision of the statistical similarity test routine, F. Rodriguez Gonzalez for his insights regarding equations (10) and (11), and N. Adam and Prof. M. Eineder for the fruitful discussions and feedback. The InSAR processing of Sentinel-1 data is performed with DLR's InSAR wide area processing (IWAP) chain.

REFERENCES

- [1] A. Ferretti, C. Prati, and F. Rocca, "Permanent scatterers in SAR interferometry," *IEEE Trans. Geosci. Remote Sens.*, vol. 39, no. 1, pp. 8–20, Jan. 2001.
- [2] B. M. Kampes, *Radar Interferometry Persistent Scatterer Technique*. The Netherlands: Springer, 2006.
- [3] R. Lanari, O. Mora, M. Manunta, J. J. Mallorqui, P. Berardino, and E. Sansosti, "A small-baseline approach for investigating deformations on full-resolution differential SAR interferograms," *IEEE Trans. Geosci. Remote Sens.*, vol. 42, no. 7, pp. 1377–1386, Jul. 2004.
- [4] A. M. Guarnieri and S. Tebaldini, "On the exploitation of target statistics for SAR interferometry applications," *IEEE Trans. Geosci. Remote Sens.*, vol. 46, no. 11, pp. 3436–3443, Nov. 2008.
- [5] A. Ferretti, A. Fumagalli, F. Novali, C. Prati, F. Rocca, and A. Rucci, "A new algorithm for processing interferometric data-stacks: SqueeSAR," *IEEE Trans. Geosci. Remote Sens.*, vol. 49, no. 9, pp. 3460–3470, Sep. 2011.
- [6] A. M. Guarnieri and S. Tebaldini, "Hybrid Cramér–Rao bounds for crustal displacement field estimators in SAR interferometry," *IEEE Signal Process. Lett.*, vol. 14, no. 12, pp. 1012–1015, Dec. 2007.
- [7] R. Touzi, A. Lopes, J. Bruniquel, and P. W. Vachon, "Coherence estimation for SAR imagery," *IEEE Trans. Geosci. Remote Sens.*, vol. 37, no. 1, pp. 135–149, Jan. 1999.
- [8] R. Bamler and P. Hartl, "Synthetic aperture radar interferometry," *Inverse Probl.*, vol. 14, no. 4, pp. R1–R54, Aug. 1998.
- [9] H. Ansari, F. De Zan, N. Adam, K. Goel, and R. Bamler, "Sequential estimator for distributed scatterer interferometry," in *Proc. IEEE Geosci. Remote Sens. Symp.*, Beijing, China, Jul. 2016, pp. 6859–6862.
- [10] S. Samiei-Esfahany, J. E. Martins, F. van Leijen, and R. F. Hanssen, "Phase estimation for distributed scatterers in InSAR stacks using integer least squares estimation," *IEEE Trans. Geosci. Remote Sens.*, vol. 54, no. 10, pp. 5671–5687, Oct. 2016.
- [11] Y. Wang and X. X. Zhu, "Robust estimators for multipass SAR interferometry," *IEEE Trans. Geosci. Remote Sens.*, vol. 54, no. 2, pp. 968–980, Feb. 2016.
- [12] F. De Zan, F. Rocca, and A. Rucci, "PS processing with decorrelating targets," in *Proc. Envisat Symp.*, 2007, pp. 1–5.
- [13] G. Fornaro, S. Verde, D. Reale, and A. Pauciuolo, "CAESAR: An approach based on covariance matrix decomposition to improve multi-baseline–multitemporal interferometric SAR processing," *IEEE Trans. Geosci. Remote Sens.*, vol. 53, no. 4, pp. 2050–2065, Apr. 2015.
- [14] H. Hua *et al.*, "The advanced rapid imaging and analysis data system: Automatic SAR data analysis for science and hazard response," in *Proc. Oral Presentations IEEE Geosci. Remote Sens. Symp.*, Milan, Italy, Apr. 2015.
- [15] P. J. Gonzalez *et al.*, "Automatic processing of SENTINEL-1 SAR data for volcano and tectonic deformation: The LICS project," in *Proc. Oral Presentations IEEE Geosci. Remote Sens. Symp.*, Milan, Italy, May 2015.
- [16] N. Adam, F. R. Gonzalez, A. Parizzi, and R. Brcic, "Wide area persistent scatterer interferometry: Current developments, algorithms and examples," in *Proc. IEEE Geosci. Remote Sens. Symp.*, Melbourne, Australia, Jul. 2013, pp. 1857–1860.
- [17] F. J. Meyer *et al.*, "Integrating SAR and derived products into operational volcano monitoring and decision support systems," *ISPRS J. Photogramm. Remote Sens.*, vol. 100, pp. 106–117, Feb. 2015.
- [18] F. De Zan and P. López-Dekker, "SAR image stacking for the exploitation of long-term coherent targets," *IEEE Geosci. Remote Sens. Lett.*, vol. 8, no. 3, pp. 502–506, May 2011.
- [19] K. Goel, N. Adam, R. Schau, and F. Rodriguez-Gonzalez, "Improving the reference network in wide-area Persistent Scatterer Interferometry for non-urban areas," in *Proc. IEEE Geosci. Remote Sens. Symp.*, Beijing, China, Jul. 2016, pp. 1448–1451.
- [20] F. Rocca, "Modeling interferogram stacks," *IEEE Trans. Geosci. Remote Sens.*, vol. 45, no. 10, pp. 3289–3299, Oct. 2007.
- [21] S.-H. Hong, S. Wdowinski, S.-W. Kim, and J.-S. Won, "Multi-temporal monitoring of wetland water levels in the Florida Everglades using interferometric synthetic aperture radar (InSAR)," *Remote Sens. Environ.*, vol. 114, no. 11, pp. 2436–2447, Nov. 2010.
- [22] A. Parizzi, X. Cong, and M. Eineder, "First results from multifrequency interferometry. A comparison of different decorrelation time constants at L, C, and X band," in *Proc. Sci. Publications, Fringe Workshop (ESA)*, Frascati, Italy, 2009, pp. 1–5.
- [23] Y. Morishita and R. F. Hanssen, "Temporal decorrelation in L-, C-, and X-band satellite radar interferometry for pasture on drained peat soils," *IEEE Trans. Geosci. Remote Sens.*, vol. 53, no. 2, pp. 1096–1104, Feb. 2015.
- [24] I. Jolliffe, *Principal Component Analysis*. Chichester, U.K.: Wiley, 2005.
- [25] F. De Zan and F. Rocca, "Coherent processing of long series of SAR images," in *Proc. IEEE Int. Geosci. Remote Sens. Symp. (IGARSS)*, vol. 3, Jul. 2005, pp. 1987–1990.
- [26] H. A. Zebker and J. Villasenor, "Decorrelation in interferometric radar echoes," *IEEE Trans. Geosci. Remote Sens.*, vol. 30, no. 5, pp. 950–959, Sep. 1992.
- [27] F. Lombardini, "Differential tomography: A new framework for SAR interferometry," *IEEE Trans. Geosci. Remote Sens.*, vol. 43, no. 1, pp. 37–44, Jan. 2005.
- [28] X. X. Zhu and R. Bamler, "Let's do the time warp: Multicomponent nonlinear motion estimation in differential SAR tomography," *IEEE Geosci. Remote Sens. Lett.*, vol. 8, no. 4, pp. 735–739, Jul. 2011.
- [29] H. A. Zebker and K. Chen, "Accurate estimation of correlation in InSAR observations," *IEEE Geosci. Remote Sens. Lett.*, vol. 2, no. 2, pp. 124–127, Apr. 2005.
- [30] R. B. D'Agostino and M. A. Stephens, Eds., *Goodness-of-Fit Techniques*. New York, NY, USA: Marcel Dekker, 1986.
- [31] A. Parizzi and R. Brcic, "Adaptive InSAR stack multilooking exploiting amplitude statistics: A comparison between different techniques and practical results," *IEEE Geosci. Remote Sens. Lett.*, vol. 8, no. 3, pp. 441–445, May 2011.
- [32] M. Schmitt, J. L. Schonberger, and U. Stilla, "Adaptive covariance matrix estimation for multi-baseline InSAR data stacks," *IEEE Trans. Geosci. Remote Sens.*, vol. 52, no. 11, pp. 6807–6817, Nov. 2014.
- [33] C.-A. Deledalle, L. Denis, F. Tupin, A. Reigber, and M. Jager, "NL-SAR: A unified nonlocal framework for resolution-preserving (Pol)(In)SAR denoising," *IEEE Trans. Geosci. Remote Sens.*, vol. 53, no. 4, pp. 2021–2038, Apr. 2015.



Homa Ansari (S'16) received the B.Sc. degree in geodesy and geodetic engineering from the University of Isfahan, Isfahan, Iran, in 2011, and the M.Sc. degree (*cum laude*) in earth oriented space science and technology from the Technical University of Munich (TUM), Munich, Germany, in 2013, with specialization on the global navigation satellite systems and microwave remote sensing. Since 2014, she has been pursuing the Ph.D. degree with the Remote Sensing Technology Institute, German Aerospace Center (DLR), Oberpfaffenhofen, Germany.

She joined the German Geodetic Research Institute, Munich, as a Research Assistant in 2012. She joined DLR as a Research Assistant in 2013. Since 2014, her Ph.D. work at DLR has been contributing to the German Helmholtz Alliance on Remote Sensing and Earth System Dynamics as well as the studies of the Tandem-L mission. In 2017, she visited the Department of Geoscience and Remote Sensing, Delft University of Technology, Delft, The Netherlands, as a Visiting Researcher. She was the recipient of the IEEE Mikio Takagi Prize, awarded for the best student paper at the 2017 IEEE International Geoscience and Remote Sensing Symposium (IGARSS), Texas, USA, 2017. Her research interests include the field of statistical signal processing, estimation theory and geodetic time series analysis with applications to the advancement of differential SAR interferometry.



Francesco De Zan was born in Lodi, Italy, in 1979. He received the master's degree in telecommunications engineering from the Politecnico di Milano, Italy, in 2004, with a focus on signal processing and remote sensing, and the Ph.D. degree in 2008, with a focus on synthetic aperture radar (SAR) interferometry with distributed and decorrelating, from the same university.

He has contributed to the development of the TOPS acquisition mode, which is currently used on ESA Sentinel-1 satellites, and collaborated with T.R.E., Milan. In 2007, he joined the Stanford Exploration Group, Stanford University, Stanford, CA, USA, as a Visiting Researcher. He joined the German Aerospace Center, Germany, in 2008, where he was with the Microwave and Radar Institute, and then with the Remote Sensing Technology Institute, contributing to the development of the Tandem-L mission concept. He was involved in aspects related to acquisition planning, performance models for deformation retrieval with InSAR and SAR tomographic applications, orbit design, the calibration of the TanDEM-X interferometer, and discovering and explaining interferometric effects which were hampering the quality of the DEM products. He was also involved in several projects for the European Space Agency related to mission design, commissioning, and application development for SAR satellites. His research interests include the field of SAR including performance of phase and delay estimators, ionospheric propagation estimation, focusing and precise geolocation of targets, soil moisture and vegetation effects, and inconsistencies in SAR interferometric phases.



Richard Bamler (M'95–SM'00–F'05) received the Diploma degree in electrical engineering, the doctorate degree in engineering, and the "Habilitation" degree in signals and systems theory from the Technical University of Munich (TUM), Munich, Germany, in 1980, 1986, and 1988, respectively.

He worked at TUM from 1981 to 1989, on optical signal processing, holography, wave propagation, and tomography. He joined the German Aerospace Center (DLR), Oberpfaffenhofen, Germany, in 1989, where he is currently the Director of the Remote Sensing Technology Institute. In 1994, he joined the Jet Propulsion Laboratory, Pasadena, CA, USA, as a Visiting Scientist, where he was involved in the preparation of the SIC-C/X-SAR missions, and in 1996, he joined the University of Innsbruck, Innsbruck, Austria, as a Guest Professor. Since 2003, he has been a Full Professor in remote sensing technology with the TUM as a double appointment with his DLR position. He is currently the Director of the Remote Sensing Technology Institute, DLR. His teaching activities include university lectures and courses on signal processing, estimation theory, and synthetic aperture radar (SAR). He, his team, and his institute have been involved in SAR and optical remote sensing, image analysis and understanding, machine learning, stereo reconstruction, computer vision, ocean color, hyperspectral image analysis, passive and active atmospheric sounding, and laboratory spectrometry. They were and are responsible for the development of the operational processors for SIR-C/X-SAR, SRTM, TerraSAR-X, TanDEM-X, PAZ, Tandem-L, ERS-2/GOME, ENVISAT/SCIAMACHY, MetOp/GOME-2, Sentinel 5p, Sentinel 4, DESIS, and EnMAP. His research interests include algorithms for optimum information extraction from remote sensing data; this involves new estimation algorithms, such as sparse reconstruction and compressive sensing for SAR, multi-/hyperspectral imaging, data fusion, and machine learning.